Design Guidelines for a Tunable SOI Based Optical Isolator in a Partially Time-Modulated Ring Resonator

Arezoo Zarif ⓘ, Khashayar Mehrany, Mohammad Memarian ⓘ, *Senior Member, IEEE,*
and Kambiz Jamshidi ⓘ, *Senior Member, IEEE*

Abstract—In this paper, we present the design guidelines for a tunable optical isolator in an SOI-based ring resonator with two small time-modulated regions. By considering a physical model, the proper geometrical and modulation parameters are designed, based on a standard CMOS foundry process. The effect of the variation of the key parameters on the performance of the isolator is explained by two counter-acting mechanisms, namely the separation between the resonance frequencies of counter-rotating modes and energy transfer to the side harmonic. We show that there is a trade-off between these parameters to obtain maximum isolation. Consequently, by applying the quadrature phase difference one can obtain the maximum separation between the resonance frequencies and hence the minimum insertion loss, while the maximum isolation is obtained at the modulation phase difference of -0.78π, which leads to a higher insertion loss. Robustness of the design is investigated through a sensitivity analysis for the fabrication variations in the distance and width of the modulated regions. We demonstrate that there is a trade-off between isolation and insertion loss, and by varying the modulation parameters, we can achieve isolation of 18 (5) dB with 7 (1.8) dB insertion loss.

Index Terms—Non-reciprocity, photonic integrated circuits, time-modulated silicon ring resonator.

I. INTRODUCTION

PHOTONIC Integrated Circuit (PIC), which is an effort to integrate multiple high-performance optical elements with different functions on a single chip, has made great progress in recent years, and offers high speed, thermal tuning ability, small footprint, large integration capacity, and compatibility with existing processing flows that allows for high yield, volume manufacturing, and low prices. Recent progress in PICs, enables the integration of various optical devices, such as passive circuits, as well as on-chip lasers, detectors, modulators and fully integrated frequency comb sources. However, on-chip integration of optical non-reciprocal devices has remained as a challenge. Optical non-reciprocal devices, such as isolators and circulators allow light transmission only in one direction while preventing the transmission in the other direction. Hence, they are essential devices in PICs, in order to stabilize lasers and reduce noise by preventing unwanted back-reflection, realizing optical transistors and logic gates for on-chip all-optical information processing systems and facilitating full duplex communications.

Traditional approach to achieve optical non-reciprocity is through the magneto-optic effect. In fact, by integrating magneto-optic materials into the waveguides and applying a strong magnetic field, one can achieve different phase shifts for the light traveling in opposite directions [1], [2], [3]. Therefore, by integrating such material in a ring resonator, one can achieve different resonant frequencies for the clockwise (c.w.) and counter-clockwise (c.c.w.) modes [4], [5], [6]. This method typically requires applying high external magnetic fields to the materials and is not compatible with complementary metal-oxide-semiconductor (CMOS) technology. Therefore, the scalability, price and volume manufacturing of this approach still remains a challenge. Furthermore, this method is intrinsically lossy, also as the magneto-optic effect is low at the optical frequencies, the resultant device is usually bulky. Moreover, as such devices usually work in the TM-like mode, mode-converter is required before and after the device, which adds to the design complexity, even further. Another method for achieving non-reciprocity is through the nonlinear effects, such as Kerr nonlinearity [7], [8], [9], [10], [11], [12]. It has been demonstrated in different platforms such as fused silica microrod resonator [7], nonlinear silicon Mach-Zehnder interferometer [8], on-chip silicon nitride ring resonator [9] and silicon ring resonator [10]. Unfortunately this method only works with high-intensity input power, which is not compatible for all of the practical applications, and is accompanied by considerable unwanted harmonics. The third approach utilizes temporal modulation [13], [14], [15], [16], [17], [18], [19], [20], [21], [22], [23], [24], [25], [26], [27], [28], [29], [30]. This approach has attracted considerable interest in recent years, because this is in principle a promising approach to realize optical isolators and circulators for PICs, as it does not require deposition of any new material or applying high power optical signals, and it can be implemented by the conventional foundry process in silicon, hence it has the potential

Arezoo Zarif and Kambiz Jamshidi are with the Integrated Photonic Devices Group, Technische Universität Dresden, 01069 Dresden, Germany (e-mail: arezoo.zarif@mailbox.tu-dresden.de; kambiz.jamshidi@tu-dresden.de).

Khashayar Mehrany and Mohammad Memarian are with the Department of Electrical Engineering, Sharif University of Technology, Tehran 11365-8639, Iran (e-mail: mehrany@sharif.edu; mmemarian@sharif.edu).

TABLE I
COMPARISON OF THE PROPOSED STRUCTURE WITH EXISTING PROPOSALS FOR INTEGRATED OPTICAL ISOLATOR

Ref	Scheme	Structure	Material	Isolation (dB)	Insertion loss (dB)	Device length (mm)
[1]	magneto-optic	Mach–Zehnder interferometer	garnet films on SOI	> 20 (dB)	20 (dB)	0.941
[6]	magneto-optic	ring	garnet films on SOI	40 (dB)	3 (dB)	0.29
[7]	Kerr non-linearity	microrod resonator	fused silica	24 (dB)	7 (dB)	1
[28]	Spatio-temporal	Ring	$Si_3N_4 + AlN$	10 (dB)	$0.1 - 1$ (dB)	0.236
[27]	Spatio-temporal	slotted waveguide	Doped Si	3 (dB)	70 (dB)	18
[29]	Temporal modulation	cascaded rings	Doped Si	16 (dB)	18 (dB)	0.22
This work	point perturbation	ring	Doped Si	18 (dB)	7 (dB)	0.008

to become manufactured in high volume. This approach has been demonstrated using various mechanisms and in different structures. Optical nonreciprocal indirect interband transition was demonstrated in a silicon waveguide, by applying a traveling wave modulation to the refractive index, to impart a shift in the momentum and frequency of the optical mode [13]. A similar effect was shown via direct interband transitions [14], [15], where the modulation only imparts the frequency shift. Another scheme is introduced by utilizing tandem phase modulators, where by applying a relative phase delay between them, one can obtain non-reciprocal frequency conversion [16], [17]. In addition to this, spatio-temporal gain-loss modulation in silicon waveguide was studied, where the modulation is applied to the conductivity to impart the intermode transition and hence obtaining non-reciprocal directional amplification [18]. As an attempt for making smaller footprint for the time-modulated devices, optical resonators were utilized to enhance the modulation strength, by confining the optical energy. Photonic transition was also shown in ring resonator [13], in a very similar manner as the one in waveguide. Another variant is the Rabi splitting in ring resonator [19], here the difference is that in the backward direction all the power is dissipated, contrary to the case of photonic transition where the power was transferred to higher frequency, therefore there is no need to an additional filter in the output. In the aforementioned papers, the transition was between different radial modes of the ring resonator. Alternatively, one can work with two degenerate counter-rotating modes and break the degeneracy of them by applying a traveling wave modulation that breaks the time reversal symmetry in a silicon ring resonator [20], [21]. Optical isolators and circulators were also demonstrated in time-modulated photonic crystal cavity array [22], [23], [24], by phase-shifting the modulation signal applied to each cavity, which induces a synthetic linear momentum in the system. It was also demonstrated in a simple macroscopic, fiber-optic resonator that the fundamental time-bandwidth product can be overcome in nonreciprocal time variant resonators [25], [26].

Despite the great deal of research in this field, there have been just a few realistic designs and experimental realizations of an optical isolator with this scheme. In fact applying the time-varying traveling wave modulation to the structure, which is a key parameter in most of the designs, is challenging to implement in practice. Although utilizing the photonic crystal cavity array alleviates the need for the spatio-temporal modulation, it adds additional complexity and more sensitivity to the fabrication imperfections, as it uses coupled photonic crystal defect cavities. Some of the recently proposed structures for integrated optical isolators using temporal modulation are

summarized in Table I, and are compared to the isolators realized with magneto-optic effect [1], [6], and nonlinear effects [7]. According to this table, magneto-optical isolators can provide high isolation; however, this is an intrinsically lossy effect and besides the requirement for deposition of the garnet film, it also requires a large footprint and applying high magnetic fields. In the optical isolator realized with Kerr non-linearity, due to the requirement of the high optical confinement, a high-Q resonator, i.e., microrod resonator, is needed which compared to the ring resonator, bears a larger footprint and less compatibility with the standard fabrication processes. Experimental realization of an optical isolator in a silicon waveguide was demonstrated via interband photonic transition in a slotted silicon waveguide, where the traveling wave modulation was sampled with a grid of 166 PN junctions [27], which besides having a large footprint and high insertion loss, is a design with high complexity. An optical isolator based on the indirect interband transition in a silicon nitride ring resonator was demonstrated, with better performance and smaller footprint, however in this structure spatio-temporal modulation is realized using acousto-optic modulation with aluminum nitride piezoelectric actuators, which requires additional step compared to the conventional CMOS fabrication process [28]. Recently an experimental proposal, based on two cascaded silicon microring modulators was presented [29], in which non-reciprocity was obtained by tuning the relative time delay between the RF driving signals and the optical delay between the modulators. Although in this method traveling wave modulation is not required and it provides even better isolation, using two ring resonators requires more space and may add more complexity to the design. On the other hand, it has higher insertion loss, compared to the isolator implemented in silicon nitride [28].

In a previously published paper the idea of the ring resonator with two time-modulated point perturbations for achieving optical non-reciprocity was presented, as a proof of concept [30], where optical isolation is obtained by breaking the degeneracy of the c.w. and c.c.w. modes, through devising the proper phase shift and distance between the modulated points. It is expected that this structure would be simpler to implement compared to the previous proposals, as it does not need the traveling wave modulation applied to the whole ring circumference. However, for practical implementation of such an isolator, we should not only change the design to comply with the design rules of the CMOS foundry process, e.g., for geometrical parameters that are dictated by the foundry process, but also we need to modify our model to account for the phenomena that happen in reality, such as free carrier absorption loss, out-of-plane radiation, bending loss, surface roughness loss, etc. In addition to this, we should

consider some restrictions that will be in the characterization stage, i.e., for the modulation parameters. It is crucial to have insight into the effect of variation of each parameter on the performance of the isolator. Not only because in the fabrication process there is always some inevitable imperfection and error, but also because due to adaptation to the fabrication rules, we may need to tune some parameters, compared to the values considered in the initial design. In this paper, such a realistic design guideline based on a CMOS-compatible silicon photonics foundry process is presented. Here we focus on the instructions for such a design by considering the realistic modulation and geometrical parameters. We study the tunability of the device and explain the effect of variation of different parameters, with two main counter-acting mechanisms, namely the separation between the resonance frequencies of counter-rotating modes and energy transfer to the side harmonic. We show that we can enhance isolation, by tuning the modulation phase difference. We examine the sensitivity of the structure to fabrication variations in the angular distance and width of the modulated regions. Our proposed structure has a small footprint and a simple design, i.e., it does not require the deposition of any new material on silicon and can be fabricated on a multi-project wafer with a commercial foundry process. Hence this work can be an important step for facilitating the fabrication and measurement of a time-modulated, compact and CMOS-compatible optical isolator.

The paper is organized as follows: In Section II Temporal Coupled Mode Theory (TCMT) is used to model our structure, and the coupling coefficients are obtained for the three-dimensional ring resonator. In Section III, we choose realistic modulation and geometrical parameters based on a CMOS-compatible silicon photonics foundry process. We use Soref equations for determining the realistic modulation parameters and find the optimum point that leads to maximum isolation. Moreover, the effect of the modulation phase on the isolation and insertion loss is evaluated. We show that we can trade off between isolation and insertion loss of the structure and classify the working point of the device into three zones, by changing the modulation parameters. In Section IV sensitivity of the performance to fabrication errors is analyzed.

II. THEORY AND MODEL

A. TCMT Formulation for the 3D Structure

The structure under study is a silicon ring resonator that is fabricated in the top silicon layer of a silicon-on-insulator (SOI) substrate and is encapsulated from above by amorphous silica, in which two small discrete regions are additionally time-modulated as a cosine function and with some phase difference (Fig. 1):

$$\Delta\varepsilon(t) = \begin{cases} \Delta\varepsilon_m \cos(\omega_m t + \Theta_1) & \phi_1 - \delta/2 \le \phi \le \phi_1 + \delta/2 \\ \Delta\varepsilon_m \cos(\omega_m t + \Theta_2) & \phi_2 - \delta/2 \le \phi \le \phi_2 + \delta/2 \end{cases} \tag{1}$$

Here, $\Delta\varepsilon(t)$ is the perturbation in relative permittivity. $\Delta\varepsilon_m$ and ω_m are modulation amplitude and angular frequency. ϕ_i, δ and Θ_i represent the position, width and modulation phase
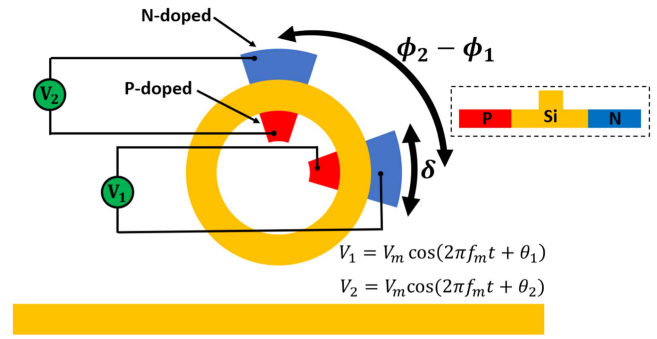

Fig. 1. Ring resonator with two time-modulated point perturbations, side coupled to the bus waveguide.

of the ith modulated region ($i = 1, 2$), where we use angular position and width, in radians. Appropriate values for the angular distance ($\phi_2 - \phi_1$), width (δ) and modulation phase difference ($\Theta_2 - \Theta_1$) of the two modulated regions, were found with the aid of TCMT [30].

We now use TCMT to obtain the spectrum of modes in such a resonator. In this approach TCMT equations governing this time perturbed ring is obtained by expanding electromagnetic fields in terms of modes of the static ring. Following this approach [31], using perturbation theory, the TCMT relations for the time-varying resonator is obtained:

$$\frac{d\boldsymbol{a}(t)}{dt} = j\boldsymbol{M}(t)\boldsymbol{a}(t) \tag{2}$$

where $\boldsymbol{a}(t)$ is a two row vector of the c.w. and c.c.w. mode amplitudes, and $\boldsymbol{M}(t)$ is the matrix representing the coupling between resonator modes:

$$\boldsymbol{a}(t) = \begin{bmatrix} a_c(t) & a_{cc}(t) \end{bmatrix}^T \tag{3}$$

$$\boldsymbol{M}(t) = \begin{bmatrix} -\frac{\omega_0}{2}\kappa_{s+}e^{j\omega_m t} - \frac{\omega_0}{2}\kappa_{s+}{}^*e^{-j\omega_m t} \\ -\frac{\omega_0}{2}\kappa_{m-}{}^*e^{j\omega_m t} - \frac{\omega_0}{2}\kappa_{m+}{}^*e^{-j\omega_m t} \end{bmatrix}$$
$$\begin{matrix} -\frac{\omega_0}{2}\kappa_{m+}e^{j\omega_m t} - \frac{\omega_0}{2}\kappa_{m-}e^{-j\omega_m t} \\ -\frac{\omega_0}{2}\kappa_{s+}e^{j\omega_m t} - \frac{\omega_0}{2}\kappa_{s+}{}^*e^{-j\omega_m t} \end{matrix} \tag{4}$$

We suppose that there is no static coupling between the modes. ω_0 is the angular resonance frequency of the static ring resonator. In the above equation, κ_{s+} represents self-coupling of each mode to itself which leads to the modulation of the mode's resonance frequency, and κ_{m+} and κ_{m-} represent the contribution of the positive (blue-shift) and negative (red-shift) modulation frequencies of the coupling between c.w. and c.c.w. modes, which are obtained by the overlap integral of the c.w. and c.c.w. modes of the unperturbed ring over the modulation regions, and can be calculated by the following equations [30]:

$$\kappa_{s+} = \Gamma\frac{\delta\Delta\varepsilon_m(e^{j\Theta_1} + e^{j\Theta_2})}{4\pi\varepsilon_s} \tag{5a}$$

$$\kappa_{m+} = \Gamma\frac{\Delta\varepsilon_m}{4\pi l\varepsilon_s}\sin(l\delta)[e^{2jl\phi_1}e^{j\Theta_1} + e^{2jl\phi_2}e^{j\Theta_2}] \tag{5b}$$

$$\kappa_{m-} = \Gamma\frac{\Delta\varepsilon_m}{4\pi l\varepsilon_s}\sin(l\delta)[e^{2jl\phi_1}e^{-j\Theta_1} + e^{2jl\phi_2}e^{-j\Theta_2}] \tag{5c}$$

where ε_s and l are the relative permittivity of silicon and the resonant mode order of the ring resonator and Γ shows mode confinement in the ring cross section:

$$\Gamma = \frac{\iint_{ring} \varepsilon |e_c|^2 r dr dz}{\iint_{entire\ space} \varepsilon |e_c|^2 r dr dz} \qquad (6)$$

where e_c is the electric field distribution of the c.w. mode of the static ring and ε is the relative permittivity profile. The degeneracy of the two modes is broken via the cross-coupling term, i.e., k_{m+} and k_{m-}. Hence due to dynamic modulation, there are two supermode spectrums with dominant c.w. and c.c.w. amplitudes, respectively. We define frequency splitting as the distance between the central resonant frequencies of the two supermodes. Therefore, the frequency splitting between the modes increases for highly confined modes. It is also inversely proportional to the mode order (l).

To analyze the optical isolator, we need to include the effect of excitation and decay into the bus waveguide, in the TCMT relations [32]:

$$\frac{d\boldsymbol{a}(t)}{dt} = (j\boldsymbol{M}(t) - \boldsymbol{\Gamma})\boldsymbol{a}(t) + \boldsymbol{K}^T \boldsymbol{s}_+ \qquad (7)$$

where $\boldsymbol{K}$ is a matrix representing the coupling coefficients from the incoming waves in waveguide ports ($\boldsymbol{s}_+$, a 2×1 vector), to the resonator, and $\boldsymbol{\Gamma}$ represents the decay rate:

$$\boldsymbol{K}^T = \begin{bmatrix} 0 & \kappa_2 \\ \kappa_1 & 0 \end{bmatrix} \qquad (8a)$$

$$\boldsymbol{\Gamma} = \begin{bmatrix} \Gamma_{11} & 0 \\ 0 & \Gamma_{22} \end{bmatrix} \qquad (8b)$$

The outgoing waves from the waveguide ports are then given by:

$$\boldsymbol{s}_- = \boldsymbol{C}\boldsymbol{s}_+ + \boldsymbol{D}\boldsymbol{a} \qquad (9)$$

where, $\boldsymbol{s}_-$ is a 2×1 vector representing outgoing waves of waveguide ports, and $\boldsymbol{C}$ and $\boldsymbol{D}$ are matrices that represent the direct coupling between waveguide ports and the coupling of the resonator to the waveguide ports, respectively:

$$\boldsymbol{C} = \begin{bmatrix} 0 & 1 \\ 1 & 0 \end{bmatrix} \qquad (10a)$$

$$\boldsymbol{D}^T = \begin{bmatrix} d_1 & 0 \\ 0 & d_2 \end{bmatrix} \qquad (10b)$$

Equations (7) and (9) are solved using harmonic balance method. According to this method, using Floquet-Bloch's theorem, temporal perturbation of the fields and also the excitation can be expanded as a sum of temporal harmonics. The dynamic equation is then expanded in terms of this series and all terms are grouped by harmonic number. Based on the orthogonality of the basis functions, the coefficients multiplying each should vanish for each harmonic number [33].
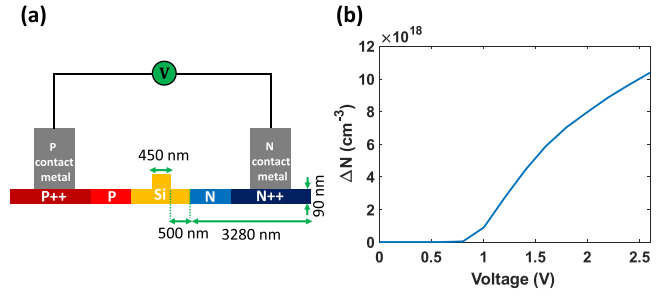

Fig. 2. (a) Schematic of the cross section of the ring resonator, simulated in Ansys Lumerical CHARGE. The background is SiO$_2$. (b) Average carrier density in the junction versus the voltage applied to the metals.

III. DESIGN CONSIDERATIONS

A. Realistic Design Parameters

In this section we consider the parameters of a CMOS-compatible silicon photonics foundry process and design the geometrical and modulation parameters of the time-modulated ring resonator based on these realistic parameters. Then we will perform a sensitivity analysis and evaluate the robustness of our design under fabrication errors. The most common method to implement modulation in silicon is through the plasma dispersion effect, in which by applying voltage to a p-i-n junction the concentration of free carriers changes and this leads to a change in refractive index and absorption coefficient of the waveguide, which is described by Soref equations [34]. The cross section of the ring resonator is a rib waveguide with a dimension of $220\,nm \times 450\,nm$ and a 90-nm slab height, as depicted in Fig. 2(a). A two-dimensional simulation in Ansys Lumerical CHARGE is used to obtain the spatial distribution of charge carriers under different values of the voltage that is applied to the junction through a metal pad on the P++ and N++ regions, as shown in Fig. 2(a). The average carrier density in the center of the waveguide is plotted versus voltage in Fig. 2(b). After obtaining the carrier density for different voltages, the change in the refractive index and absorption is calculated with Soref equations.

To calculate the bending loss of the ring resonator, cross section of the ring resonator (as depicted in Fig. 2(a)) is simulated via Ansys Lumerical MODE, using Finite Difference Eigenmode (FDE) solver, which calculates the modes of the bent waveguide, by solving Maxwell's equations on a cross section of the waveguide. A simulation region of $5.8\,\mu m \times 4.5\,\mu m$ with 400 mesh cells in each direction, is considered.

For choosing the silicon ring radius, two issues should be considered. First it should be large enough to provide working with small bending loss, and second it should be small enough to have acceptable frequency splitting. As an explanation, by decreasing the ring radius, the bending loss, caused by total internal reflection of the light at the bend interface, increases. Therefore the resonance bandwidth is broadened. On the other hand, increasing the ring radius reduces the frequency splitting between c.w. and c.c.w. modes. In fact larger radius is equivalent to larger mode order (l) and according to (5), increasing the
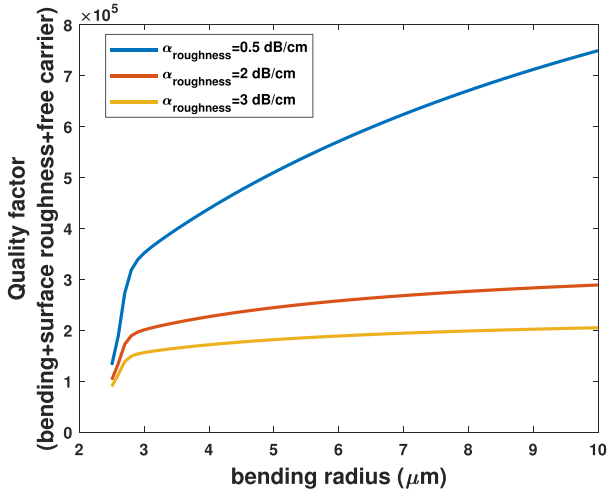
Fig. 3.   Intrinsic quality factor of the ring resonator versus bending radius.
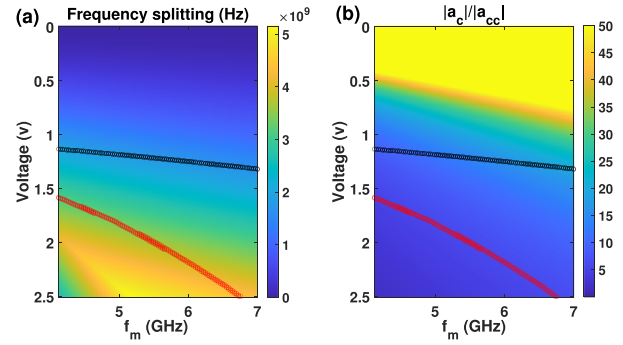

Fig. 4.   (a) Frequency-splitting between two supermodes, and (b) ratio of c.w. to the c.c.w. mode at the central frequency of supermode spectrum, versus modulation frequency and the voltage amplitude. Black and red curves represent points where the frequency-splitting equals BW and $f_m - BW$, respectively. Here BW and f_m are the intrinsic resonance linewidth and the modulation frequency, respectively.

mode order reduces the coupling coefficient between c.w. and c.c.w. modes (κ_{m-} or κ_{m+}). Therefore, the frequency splitting will decrease. Hence, there is a trade-off between the bending loss and the frequency splitting, for choosing the ring radius. The other two mechanisms of the loss in this ring resonator are free carrier absorption and surface roughness loss. Assuming a change in the refractive index of $\Delta n = 0.004$, the absorption caused by the free carriers ($\alpha_{carrier}$) is calculated by Soref equations [34]. The absorption coefficient caused by the bending loss (α_{bend}) is calculated via numerical simulations in Ansys Lumerical MODE. Therefore, the total quality factor (Q_T) of the ring resonator includes the contribution of the quality factor of the ring without electro-optic modulation (Q_{static}) and quality factor of the ring due to free carrier absorption loss ($Q_{carrier}$), and is calculated as:

$$Q_{static} = \frac{2\pi n_g}{\lambda(\alpha_{bend} + \alpha_{roughness})} \tag{11a}$$

$$Q_{carrier} = \frac{2\pi^2 n_g}{\lambda \alpha_{carrier} \delta} \tag{11b}$$

$$Q_T = \left(\frac{1}{Q_{static}} + \frac{1}{Q_{carrier}}\right)^{-1} \tag{11c}$$

here n_g and λ are the group index and the resonance wavelength, respectively. Also $\alpha_{roughness}$ represents the absorption caused by the surface roughness loss. According to Fig. 3, the intrinsic quality factor increases as the ring radius increases. For radii larger than $4\,\mu$m, increasing the radius has negligible effect on the quality factor, for $\alpha_{roughness} = 2\,$dB/cm and $\alpha_{roughness} = 3\,$dB/cm. For $\alpha_{roughness} = 0.5\,$dB/cm, as the surface roughness loss becomes comparable to the free carrier absorption loss, by increasing radius, and hence decreasing the modulation region, the free carrier absorption loss decreases, and the quality factor increases.

We consider some points, first we assume working with the $4\,\mu$m ring. Second, we suppose the quadrature phase difference between the modulated regions, i.e., $\Theta_2 - \Theta_1 = -\frac{\pi}{2}$.

The distance between the modulated regions is chosen in a way that together with the quadrature phase condition satisfies the condition $|\kappa_{m+}| \gg |\kappa_{m-}|$. The width of the modulated regions is chosen to maximize $|\kappa_{m+}|$. These assumptions leads to maximum frequency splitting [30]. Then we find the optimum point to achieve maximum optical isolation in the next step. For this purpose, we use the scheme used in [30] and consider two parameters to quantify the performance of the isolator, namely frequency splitting and the ratio of the c.w. to the c.c.w. modes for the central harmonics of the two supermodes. These two parameters are plotted versus modulation frequency (f_m) and the voltage amplitude in Fig. 4. Surface roughness absorption coefficient of down to $\alpha = 0.5\,$dB/cm is considered [35]. The operating point can be between the black and red curves in Fig. 4 which represent points where frequency-splitting equals BW and $f_m - BW$, respectively. Here BW and f_m are the intrinsic resonance linewidth and the modulation frequency, respectively. As an explanation, due to the temporal harmonic modulation, this structure has two supermode spectrums that are obtained by solving (2). Each supermode consists of c.w. and c.c.w. harmonics that are equally spaced with a distance of f_m. Assuming working in the central harmonic of the supermode, the frequency splitting should be such that the spectrum is completely separated from the neighboring counter-rotating spectrums. In fact BW and $f_m - BW$ determine the minimum and maximum acceptable frequency splitting, which ensures both the separation between the zeroth order harmonics and the separation between the central harmonic and the first side harmonic. The optimum point which gives maximum isolation, occurs at a point in this region, which has the maximum ratio of the c.w. to the c.c.w. mode. Using this scheme, we choose the optimum working point that gives maximum isolation, while maintaining an insertion loss of -3dB. Forward and backward power transmission spectra for the optimum point are plotted in Fig. 5, assuming surface roughness loss of $\alpha = 0.5\,$dB/cm.

The modulation frequency, the voltage amplitude and the intrinsic resonance linewidth are $f_m = 7\,$GHz, V = 1.321 V and $BW = 950\,$MHz for this point. These spectra indicate
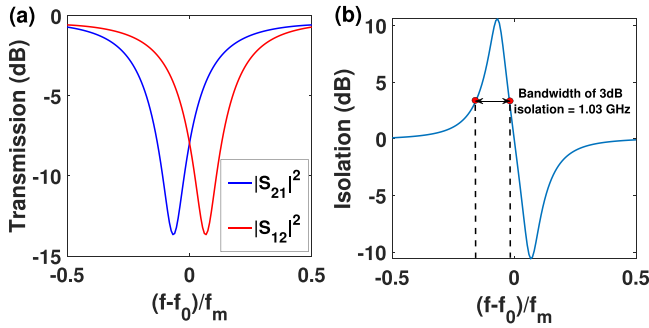
Fig. 5. (a) Forward (S_{12}) and backward (S_{21}) power transmission spectrum of the time-modulated ring resonator for the optimum point and, (b) optical isolation ($\frac{|S_{12}|^2}{|S_{21}|^2}$) versus frequency for the optimum point. The bandwidth at which the isolator works with the isolation of 3 dB and more is 1.03 GHz. f_0 is the resonance frequency of the static ring resonator.
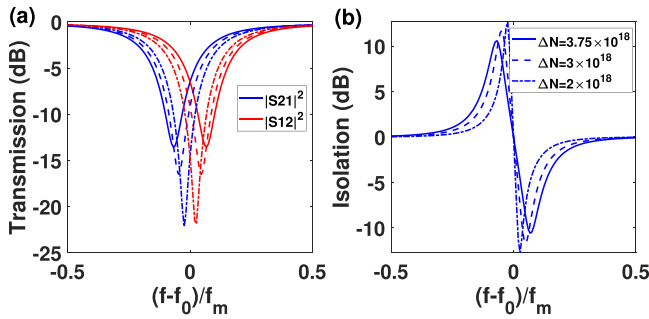

Fig. 6. (a) Forward (S_{12}) and backward (S_{21}) power transmission spectra of the time-modulated ring resonator for three different values of the change in the carrier density ΔN. (b) Optical isolation versus frequency for three different values of the change in the carrier density ΔN.

non-reciprocal transmission in this structure, and an isolation of 10.54 dB and an insertion loss of -3.02 dB is obtained, at the resonance frequency. Isolation ($|S_{12}|^2/|S_{21}|^2$) is plotted in Fig. 5(b) versus frequency. According to this figure, the bandwidth at which this device works with the isolation of 3 dB and higher, is 1.03 GHz.

It is worth mentioning that as shown in Fig. 4, the working points on the black curve have approximately the same ratio of c.w. to the c.c.w. mode, this leads to a tunable optical isolator where by varying the voltage and modulation frequency, the optimum working point can be tuned on this curve.

B. Tunability

To demonstrate the tunability of this device, transmission spectrum is plotted for three different values of the modulation voltage and the corresponding change in the carrier density in Fig. 6. According to Fig. 6, by decreasing the voltage to V = 1.233 V ($\Delta N = 3 \times 10^{18}$), isolation, insertion loss, frequency splitting and the intrinsic resonance linewidth are 12.61 dB, -3.86 dB, 657 MHz and 789 MHz, respectively, and by decreasing it further to V = 1.121 V ($\Delta N = 2 \times 10^{18}$), isolation, insertion loss, frequency splitting and the intrinsic resonance

linewidth are 16.09 dB, -5.96 dB, 333 MHz and 573 MHz, respectively. In fact by decreasing the carrier density, the modulation amplitude decreases and according to (5), it will decrease the self-coupling term, i.e., κ_{s+}, which decreases the power transfer to the side harmonics. Therefore most of the energy remains in the central harmonic and couples back to the waveguide and destructively interferes with the optical wave in the waveguide. This leads to the decrease in the backward transmission, hence the isolation is increased. On the other hand, decreasing the modulation amplitude, decreases the cross-coupling term (κ_{m+}), which decreases the frequency splitting. Therefore the forward transmission decreases and hence the insertion loss is increased. Here and in the rest of the paper, when discussing changes in insertion loss, we mean the changes in absolute value of it.

Then we consider the phase difference of the two modulated regions ($\Theta_2 - \Theta_1$ as shown in Fig. 1), and its effect on the key parameters, namely, isolation and insertion loss. According to (2)–(4), performance of the isolator is mainly determined by the cross-coupling terms, i.e., $|\kappa_{m+}|$ and $|\kappa_{m-}|$, as well as the self-coupling term, i.e., $|\kappa_{s+}|$. In fact, if there was no self-coupling, each of the supermodes consists only of one frequency component, i.e., the central harmonic. So each of the supermodes shrinks to one harmonic. However, by increasing the self-coupling term, some power is transferred to the side harmonics. Therefore, smaller portion of the power couples back to the waveguide in the central harmonic to destructively interfere with the optical wave in the waveguide, and to decrease the output. Therefore, by increasing the self-coupling term, the output power at resonance frequency, which is the backward transmission of the isolator, increases, and this results in the decrease of the optical isolation. Next we consider the effect of the cross-coupling terms on the performance. Neglecting the effect of the self-coupling term, considering $\kappa_{s+} = 0$, if $\kappa_{m+} >> \kappa_{m-}$, according to (2)–(4), the c.w. mode will have a blue-shift equal to the modulation frequency (f_m). Therefore, the frequency splitting is maximized under this condition. When the $|\kappa_{m+}|/|\kappa_{m-}|$ is decreased, the frequency splitting decreases. This will result in the decrease of the forward transmission of the optical isolator and hence the decreased isolation and increased insertion loss. The same interpretation applies for $|\kappa_{m-}|/|\kappa_{m+}|$, but here the c.w. mode will undergo a red-shift. This can be verified in Fig. 7. Here we consider $\Theta_1 = 0$. According to Fig. 7, at $\Theta_2 = -\pi/2$ ($\Theta_2 = \pi/2$), $|\kappa_{m+}|/|\kappa_{m-}|$ ($|\kappa_{m-}|/|\kappa_{m+}|$) is maximized, therefore in this point the frequency splitting and hence the forward transmission is maximized. Therefore, here the absolute value of the insertion loss is minimized. On the other hand, the minimum of the self-coupling term is at $\Theta_2 = \pm\pi$. As a result, at this point least energy is transferred to the side harmonic, and all the back coupled energy to the waveguide is in the central harmonic and destructively interferes with the power in the waveguide. Hence the backward transmission is minimized. The optimum point for maximum isolation happens somewhere between the $\Theta_2 = -\pi/2$ and $\Theta_2 = -\pi$. (or between $\Theta_2 = \pi/2$ and $\Theta_2 = \pi$, for the red-shift of the c.w. mode). It means that there is a trade-off between these two factors, for maximum isolation. The phase difference that we already
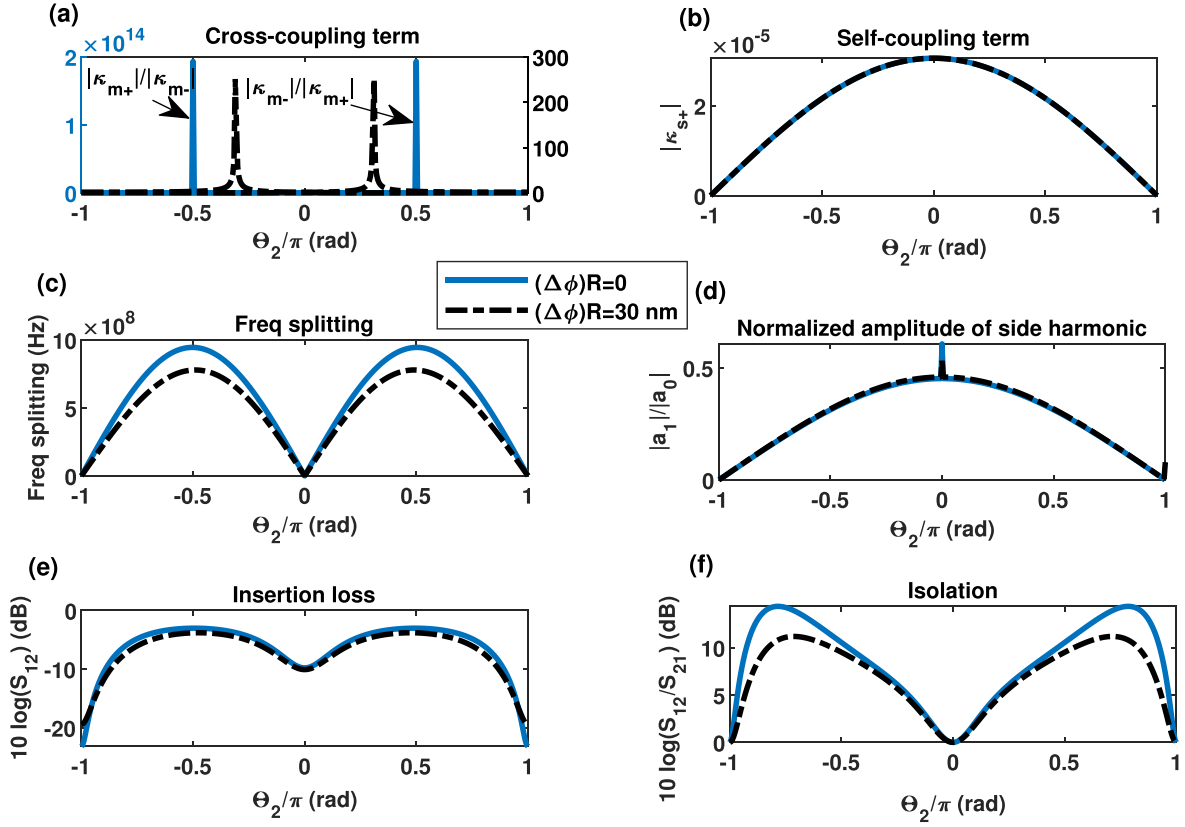
Fig. 7. (a) Cross-coupling term, (c) frequency splitting and (e) insertion loss, versus modulation phase of the second region, maximum point for these plots occurs at $\Theta_2 = \pm\pi/2$. (b) Self-coupling term and (d) normalized amplitude of the side harmonic, versus modulation phase of the second region, which has minimum point at $\Theta_2 = \pm\pi$. (f) Isolation versus Θ_2. Maximum isolation of 14.36 dB occurs at $\Theta_2 = -0.78\pi$ (or $\Theta_2 = 0.78\pi$, for the red-shift of the c.w. mode). The blue solid line represents the ideal condition and the black dash-dotted line represents the scenario that there might be a 30 nm shifting of the second region along the circumference of the ring due to fabrication imperfections ($(\Delta\phi)R = 30$ nm), where $\Delta\phi = \phi_2 - \phi_i$, and $\phi_i = \frac{(2l\phi_1 + 2n\pi + \frac{\pi}{2})}{2l}$, and due to the symmetry, we consider $\phi_1 = 0$.

considered in the previous sections was based on obtaining maximum cross-coupling term. In fact by considering the quadrature phase difference we maximize the frequency splitting and hence minimize the absolute value of insertion loss. However, it is observed (according to Fig. 7(f)) that actually we can achieve better isolation, if we work at $\Theta_2 = -0.78\pi$ (or $\Theta_2 = 0.78\pi$, for the red-shift of the c.w. mode). At this new Θ_2, isolation is increased to 14.36 dB and insertion loss is -5.52 dB. At this point, the absolute value of the insertion loss is increased.

Next, we plot the transmission spectrum for $\Theta_2 - \Theta_1 = -\frac{\pi}{2}$ and also for the scenarios that $\Theta_2 - \Theta_1$ has a deviation equal to $\Delta\Theta$ from this value. According to Fig. 8, the isolation, insertion loss and frequency splitting will be 7.98 dB, -3.46 dB and 836 MHz, respectively for a 30 percent increase in the phase difference of the two regions. By increasing the variation to 50 percent, the isolation, insertion loss and frequency splitting will be 6.10 dB, -4.44 dB and 660 MHz, respectively.

Next, we demonstrate that we can trade off between the optical isolation and insertion loss, by varying the modulation parameters, i.e., Voltage (equivalently ΔN), f_m and Θ_2. As a consequence, we will classify the working regimes, into three zones. We sweep the modulation frequency and voltage and plot the isolation and insertion loss for different modulation phases,
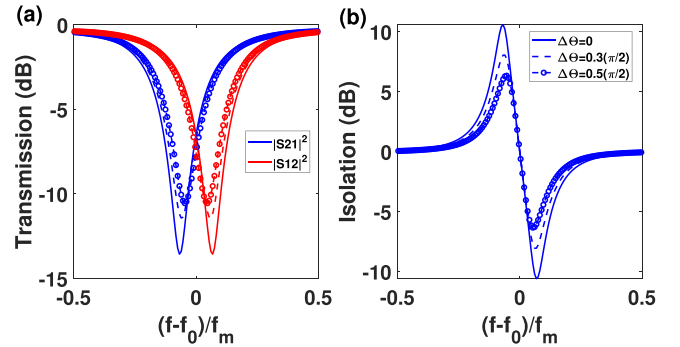

Fig. 8. (a) Forward (S_{12}) and backward (S_{21}) transmission spectra, and b) isolation versus frequency, for $\Theta_2 = -\frac{\pi}{2}$ and for the scenario that there is a variation of $\Delta\Theta = 0.3(\frac{\pi}{2})$ and $\Delta\Theta = 0.5(\frac{\pi}{2})$ in the phase difference between the two regions, where $\Delta\Theta = \Theta_2 + \frac{\pi}{2}$.

i.e., $\Theta_2 = -\frac{\pi}{2}$ and $\Theta_2 = -0.78\pi$. As shown in Fig. 9, each range of isolation corresponds to a range for insertion loss, and one can achieve higher isolation at the cost of higher insertion loss. Consequently, one can classify the working point into three zones. In the first zone, the isolator works with small insertion loss. Working at this zone can be useful for the applications
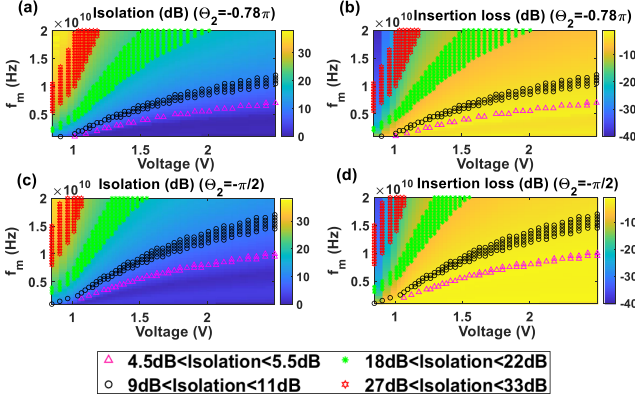
Fig. 9. (a) Isolation and (b) insertion loss versus modulation frequency f_m and voltage amplitude, for $\Theta_2 = -0.78\pi$. (c) Isolation and (d) insertion loss versus modulation frequency f_m and voltage amplitude, for $\Theta_2 = -\pi/2$.

TABLE II
COMPARISON BETWEEN $\Theta_2 = -\pi/2$ AND $\Theta_2 = -0.78\pi$, FOR THE WORKING POINT IN THE SECOND ZONE, AND MODULATION FREQUENCY OF $f_m = 7$ GHz

Θ_2 (rad)	ΔN (cm^{-3})	Isolation (dB)	Insertion loss (dB)
$-\pi/2$	1.5×10^{18}	18.26	-7.88
-0.78π	2.25×10^{18}	18.62	-8.38

TABLE III
COMPARISON BETWEEN $\Theta_2 = -\pi/2$ AND $\Theta_2 = -0.78\pi$, FOR THE WORKING POINT IN THE SECOND ZONE, AND MODULATION AMPLITUDE OF $\Delta N = 3 \times 10^{18}$ CM^{-3}

Θ_2 (rad)	f_m (GHz)	Isolation (dB)	Insertion loss (dB)
$-\pi/2$	12	18.16	-6.97
-0.78π	8.5	18.22	-7.86

where very low insertion loss is needed. Therefore, we choose the quadrature modulation phase, i.e., $\Theta_2 = -\frac{\pi}{2}$, and a point with moderate isolation of 4.63 dB, but very good insertion loss of -1.76 dB can be achieved at this point. In the second zone, high isolation is needed, but on the other hand higher insertion loss can be tolerated. Hence, we can work with either $\Theta_2 = -\frac{\pi}{2}$ or $\Theta_2 = -0.78\pi$. According to Table II and Table III, to achieve the same isolation ratio, one can work with smaller modulation amplitude and obtain better insertion loss, for $\Theta_2 = -\frac{\pi}{2}$. On the other hand, one can work at smaller modulation frequency, but achieve higher insertion loss, for $\Theta_2 = -0.78\pi$. There is also a third zone, between the aforementioned zones, where the device works with moderate isolation of 10.54 dB, and insertion loss of -3.02 dB, for $\Theta_2 = -\frac{\pi}{2}$, as obtained in Section III-A.

IV. SENSITIVITY ANALYSIS

In this section robustness of our design to the fabrication variations of parameters such as, angular distance ($\phi_2 - \phi_1$ in Fig. 1) and width (δ in Fig. 1) of the modulated regions will be evaluated.

A. Angular Distance Variation

We choose the quadrature phase difference ($\Theta_2 - \Theta_1 = -\frac{\pi}{2}$), which minimizes the absolute value of insertion loss, and proceed to investigate the effect of the fabrication errors on the performance of the isolator. First we consider fabrication error in the distance between the two points, i.e., $\phi_2 - \phi_1$ as shown in Fig. 1. According to (5), the condition $\Theta_2 - \Theta_1 = -\pi/2$ together with $2l\phi_2 = 2l\phi_1 + 2n\pi + \frac{\pi}{2}$ leads to the condition $|\kappa_{m+}| >> |\kappa_{m-}|$, hence the frequency splitting is maximized and the c.w. spectrum will undergo a blue-shift. Without loss of generality, and due to the symmetry, we consider $\phi_1 = 0$. For the case that ϕ_2 is deviated from the ideal value $\phi_i = \frac{(2l\phi_1 + 2n\pi + \frac{\pi}{2})}{2l}$, $|\kappa_{m+}|/|\kappa_{m-}|$ is decreased, hence the frequency splitting and therefore, the forward transmission decreases. Therefore, it will degrade both the isolation and insertion loss. However the self-coupling coefficient $|\kappa_{s+}|$ and therefore the amplitude of the side harmonic is independent from the ϕ_2, hence, as explained earlier the backward transmission will not change. These predictions can be verified in Fig. 10. According to (5), if the variation of ϕ_2 is equal to $\frac{\pi}{2l}$, $|\kappa_{m+}|$ and $|\kappa_{m-}|$ and hence the split c.w. and c.c.w. modes are swapped. Therefore according to Fig. 10, frequency splitting is a periodic function of ϕ_2, with the period $\frac{\pi}{2l}$. Also, as the forward transmission is determined by the frequency splitting, and since the backward transmission does not change by varying ϕ_2, insertion loss and isolation are also periodic functions, with the same period. Another interesting point, is that at the points where $|\kappa_{m+}| = |\kappa_{m-}|$, frequency splitting is minimized, since according to (2)–(4), in this condition c.w. and c.c.w. modes have the same frequency shift.

Next, the transmission spectra are plotted for the scenario that there are some fabrication imperfections in the distance between the two points. The isolation, insertion loss, and frequency splitting will be 7.17 dB, -5.97 dB, and 510 MHz, respectively for a $\Delta\phi = 0.0125$ rad (50 nm shifting of the second region along the circumference of the ring due to fabrication imperfections). Here $\Delta\phi = \phi_2 - \phi_i$, where $\phi_i = \frac{(2l\phi_1 + 2n\pi + \frac{\pi}{2})}{2l}$ is the ideal value of ϕ_2. By decreasing this value to $\Delta\phi = 0.0075$ rad (equivalently 30 nm shift), the isolation, insertion loss, and frequency splitting will be 9.52 dB, -3.81 dB, and 781 MHz, respectively. According to Fig. 11, here the backward transmission does not change, and the degradation of the isolation is originated from the decreased frequency splitting and hence the decreased forward transmission, caused by the deviation from the aforementioned condition, i.e., $2l\phi_2 = 2l\phi_1 + 2n\pi + \frac{\pi}{2}$.

To obtain better insight of the effect of these parameters, Θ_2 and $\Delta\phi$ are swept together. As shown in Fig. 12, frequency splitting is maximized in the points where $\Theta_2 = \pm\frac{\pi}{2}$ and $2l\phi_2 = 2l\phi_1 + 2n\pi + \frac{\pi}{2}$. Therefore these points represent the zone where the absolute value of the insertion loss is minimized. As shown in Fig. 12(a) and (f), at the points where $2l\phi_2 = 2l\phi_1 + 2n\pi + \pi$, cross-coupling term has equal red-shift and blue-shift contributions, i.e., $|\kappa_{m+}| = |\kappa_{m-}|$. Consequently, isolation will be zero in this region. At $\Theta_2 = \pm\pi$ and $\Theta_2 = 0$, frequency splitting is zero, hence the isolation will also be zero in this zone. As $\Delta\phi$ moves away from $\Delta\phi = -\frac{\pi}{4l}$, the zone of maximum isolation moves to the smaller $|\Theta_2|$.
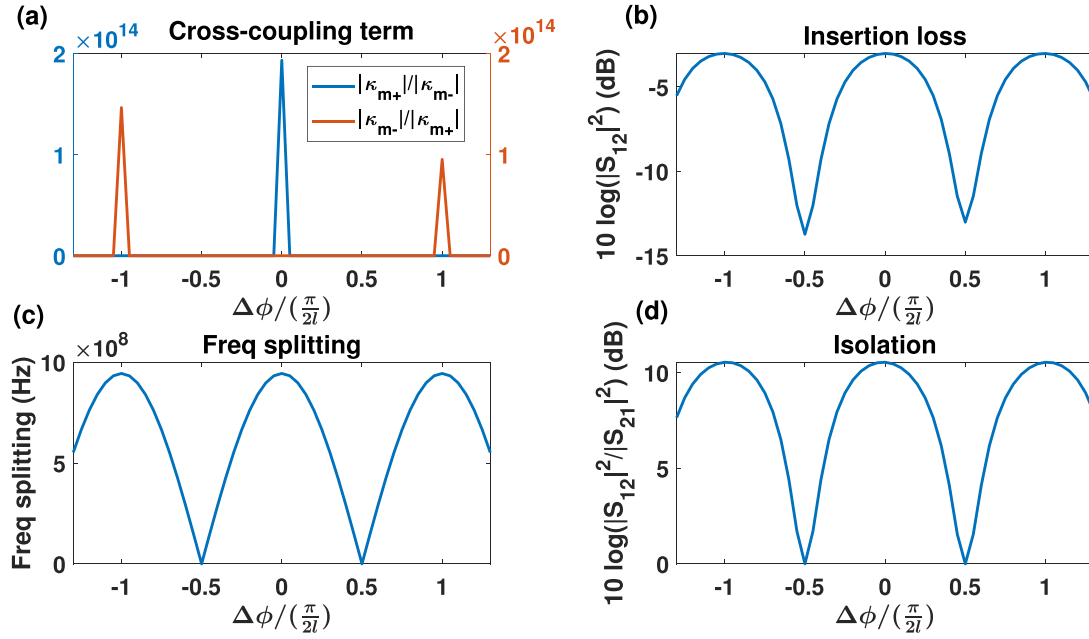
Fig. 10. (a) Cross-coupling term, (b) insertion loss, (c) frequency splitting, and (d) isolation versus position of the second region (position of the first region is $\phi_1 = 0$), the maximum point for these plots occurs at $\Delta\phi = 0$, where $\Delta\phi = \phi_2 - \phi_i$, and $\phi_i = \frac{(2l\phi_1 + 2n\pi + \frac{\pi}{2})}{2l}$, and is repeated with the period $\frac{\pi}{2l}$.
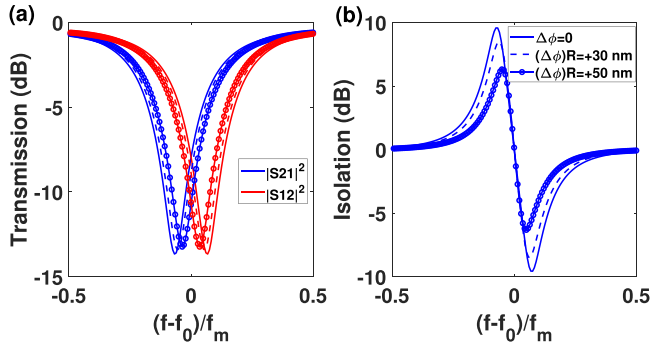

Fig. 11. (a) Forward (S_{12})) and backward (S_{21}) transmission spectra, and b) isolation versus frequency, for $\phi_2 = \phi_i$ and for the scenario that there is a variation of $(\Delta\phi)R = 30$ nm and $(\Delta\phi)R = 50$ nm in the distance between the two regions, where $\Delta\phi = \phi_2 - \phi_i$.

Therefore, if there is some variation in the distance between the two regions, it can be compensated, to some extent, by tuning the modulation phase difference accordingly.
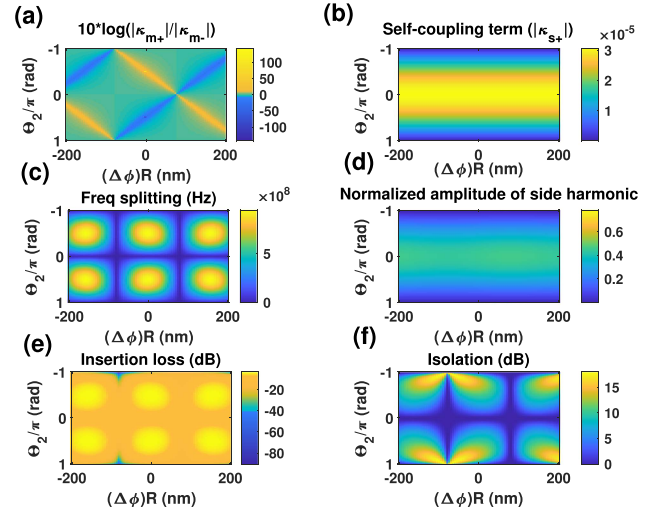

Fig. 12. (a) Cross-coupling term, (b) self-coupling term, (c) frequency splitting, (d) normalized amplitude of the side harmonic, (e) insertion loss, and (f) isolation versus Θ_2 and $\Delta\phi$. Maximum frequency splitting and insertion loss is obtained at quadrature phase, for Θ_2. Minimum self-coupling term and amplitude of the side harmonic is obtained at $\Theta_2 = \pm\pi$.

B. Width Variation

Other important parameter is the width of the modulated regions (δ). According to (5), the cross-coupling term is a sinusoidal function of δ, and is maximized at $\delta_i = \frac{\pi}{2l}$. As the width of the modulated regions is deviated from this value, the frequency splitting which is proportional to the cross-coupling term, is reduced, as plotted in Fig. 13. On the other hand, by reducing the width of the modulated regions, the free carrier absorption loss decreases and hence the linewidth reduces. Therefore, the

absolute value of insertion loss is minimized at a width between δ_i and the smallest modulation width. Moreover, according to (5), by increasing the modulation width, the self-coupling term, which represents the modulation of the resonance frequency, increases. This broadens the supermode spectrum and increases the amplitude of the side harmonic, as shown in Fig. 13. Under this condition, some of the energy of the resonating ring couples to the side harmonics, and smaller portion of the energy is coupled back to the waveguide in the central frequency,
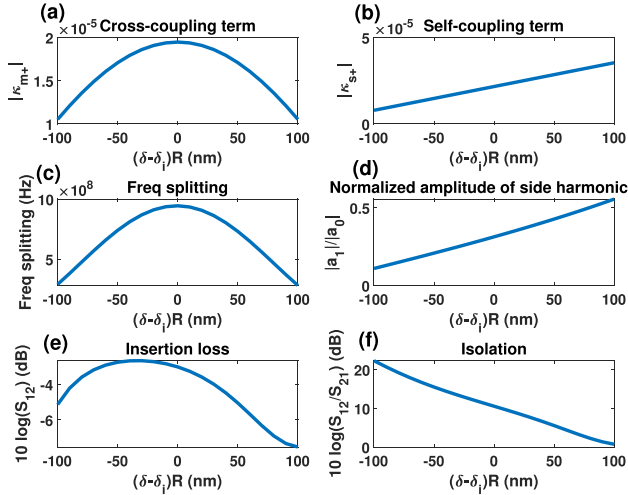
Fig. 13.   (a) Cross-coupling term and (c) frequency splitting are maximized at $\delta_i = \frac{\pi}{2l}$. (e) Insertion loss which its absolute value is minimized at another δ, due to the increase of the linewidth by increasing the modulation regions. (b) Self-coupling term and (d) the normalized amplitude of the side harmonic, which increases by increasing δ, and (f) isolation which decreases by increasing δ.
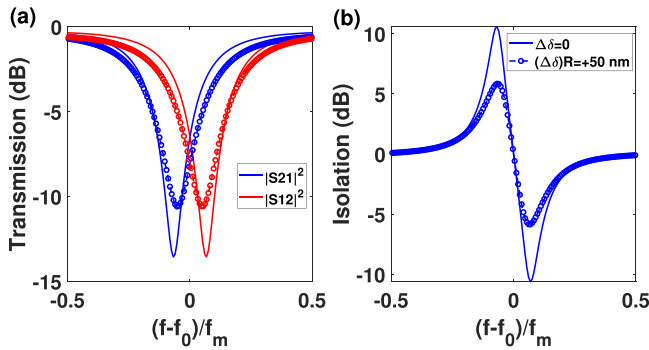

Fig. 14.   (a) Forward (S_{12}) and backward (S_{21}) transmission spectra, and b) isolation versus frequency, for $\delta = \delta_i$ and for the scenario that there is a variation of 50 nm in the width of the modulated regions (($\Delta\delta)R = +50$ nm), where $\Delta\delta = \delta - \delta_i$.

therefore the transmission, which had to be extinct due to the destructive interference with the wave in the waveguide, is not dropped completely. Consequently, the backward transmission increases, which leads to further decrease in the isolation. Next, transmission spectrum is plotted for the scenario that there is a 50 nm error in the width of the modulated regions, compared to the ideal value, i.e., δ_i. According to Fig. 14, transmission spectrum is broadened by increasing δ, due to the increase in the free carrier absorption loss, and the isolation, insertion loss, frequency splitting and the intrinsic resonance linewidth will be 5.54 dB, −5.05 dB, 741 MHz and 1.21 GHz, respectively for a 50 nm change in the width of the modulated regions, i.e., $(\delta - \delta_i)R$. Results of this section can be useful both in the design and measurement stages, as we investigated the effect of each parameter on the key performance metrics, i.e., isolation, insertion loss and frequency splitting.

V. CONCLUSION

In this paper, design guidelines for a tunable optical isolator in a silicon ring resonator with two time-modulated parts has been presented. The design is based on a CMOS compatible silicon photonics foundry process. It has been demonstrated that there is a trade-off between the resonance bandwidth and frequency splitting for choosing the ring radius. Isolation, insertion loss and frequency splitting of 10.54 dB, −3.02 dB and 950 MHz have been achieved for a modulation frequency and voltage amplitude of $f_m = 7$ GHz and V=1.321 V, respectively, and for $\Theta_2 - \Theta_1 = -\frac{\pi}{2}$. The bandwidth at which this device works with the isolation of 3 dB and higher, is 1.03 GHz. It has been demonstrated that the two main parameters that affect the performance, are the amplitude of the cross-coupling and self-coupling terms in TCMT equations, that determine the frequency splitting and energy transfer to the side harmonics, respectively. In fact, frequency splitting determines the forward transmission and amplitude of the side harmonics affects the backward transmission of the isolator. We have shown that by applying the 90 degrees phase difference between the modulated points, one can obtain the maximum frequency splitting and hence the lowest insertion loss, while the maximum isolation of 14.36 dB occurs for $\Theta_2 = -0.78\pi$, which results in a higher insertion loss of −5.52 dB. In other words there is a trade-off between the maximum cross-coupling and the minimum self-coupling terms, to obtain the maximum isolation. It has been shown that the isolation, insertion loss, and frequency splitting will be 7.98 dB, −3.46 dB, and 836 MHz, respectively for a 30 percent increase in the phase difference of the two regions, i.e., $\Delta\Theta$, and they will be 6.10 dB, −4.44 dB, and 660 MHz, respectively, by increasing the variation to 50 percent. Tunability of the device under variations of the change in the carrier density has been demonstrated and explained by similar reasoning. In fact by decreasing the ΔN to 3×10^{18}, isolation, insertion loss, frequency splitting and the intrinsic resonance linewidth are 12.61 dB, −3.86 dB, 657 MHz, and 789 MHz, respectively, and by decreasing it further to $\Delta N = 2 \times 10^{18}$, isolation, insertion loss, frequency splitting, and the intrinsic resonance linewidth are 16.09 dB, −5.96 dB, 333 MHz, and 573 MHz, respectively. The sensitivity of the device performance to the imperfections has been analyzed. It has been shown that variation in the distance of the regions degrades the performance by changing the frequency splitting and hence the forward transmission and for a 30 nm shifting of the second region along the circumference of the ring, i.e., $(\Delta\phi)R$, the isolation, insertion loss, and frequency splitting will be 9.52 dB, −3.81 dB and 781 MHz, respectively. By increasing this value to 50 nm, the isolation, insertion loss and frequency splitting will be 7.17 dB, −5.97 dB, and 510 MHz, respectively.

It has been observed that for $\Theta_2 = 0$ and $\Theta_2 = \pm\pi$ and also at the points where $2l\phi_2 = 2l\phi_1 + 2n\pi + \pi$, cross-coupling term has equal red-shift and blue-shift contributions, i.e., $|\kappa_{m+}| = |\kappa_{m-}|$. Consequently, isolation will be zero in this region. Isolation, insertion loss, frequency splitting and the intrinsic resonance linewidth will be 5.54 dB, −5.05 dB, 741 MHz and 1.21 GHz, respectively for a 50 nm change in the width of

the modulated regions, i.e., $(\delta - \delta_i)R$. Moreover, based on the analysis, there is a trade-off between insertion loss and isolation, by tuning the modulation parameters, and it has been shown that an insertion loss of only -1.8 dB can be obtained for an isolation of 5 dB whereas an isolation of up to 18 dB can be achieved if an insertion loss of -7 dB can be tolerated. Our proposed structure is simple to implement and has a small footprint, as it uses only one ring resonator with two small, modulated regions. Moreover, it is completely compatible with the conventional CMOS fabrication processes. We believe that this work can pave the way toward the fabrication of a non-magnetic, CMOS-compatible, and compact optical isolator.

References

[1] D. Huang, P. Pintus, Y. Shoji, P. Morton, T. Mizumoto, and J. E. Bowers, "Integrated broadband Ce: YIG/Si Mach–Zehnder optical isolators with over 100 nm tuning range," *Opt. Lett.*, vol. 42, no. 23, pp. 4901–4904, 2017.

[2] B. J. Stadler and T. Mizumoto, "Integrated magneto-optical materials and isolators: A review," *IEEE Photon. J.*, vol. 6, no. 1, Feb. 2014, Art. no. 0600215.

[3] M. Li et al., "Design of a broadband and low loss TM magneto-optical waveguide isolator based on lithium niobate on insulator," *IEEE Photon. J.*, vol. 13, no. 2, pp. 1–11, Apr. 2021.

[4] Y. Zhang et al., "Monolithic integration of broadband optical isolators for polarization-diverse silicon photonics," *Optica*, vol. 6, no. 4, pp. 473–478, 2019.

[5] Y. Kawaguchi, A. Alù, and A. B. Khanikaev, "Non-reciprocal parity-time symmetry breaking based on magneto-optical and gain/loss double ring resonators," *Opt. Mater. Exp.*, vol. 12, no. 4, pp. 1453–1460, 2022.

[6] Q. Du et al., "Monolithic on-chip magneto-optical isolator with 3 dB insertion loss and 40 dB isolation ratio," *ACS Photon.*, vol. 5, no. 12, pp. 5010–5016, 2018.

[7] L. Del Bino, J. M. Silver, M. T. Woodley, S. L. Stebbings, X. Zhao, and P. Del'Haye, "Microresonator isolators and circulators based on the intrinsic nonreciprocity of the Kerr effect," *Optica*, vol. 5, no. 3, pp. 279–282, 2018.

[8] M. Ding et al., "Silicon nonlinear switch as a conditional circulator for monostatic LiDAR systems," *Photon. Res.*, vol. 10, no. 2, pp. 426–432, 2022.

[9] A. D. White et al., "Integrated passive nonlinear optical isolators," 2022, *arXiv:2206.01173*.

[10] K. Y. Yang et al., "Inverse-designed non-reciprocal pulse router for chip-based LiDAR," *Nature Photon.*, vol. 14, no. 6, pp. 369–374, 2020.

[11] Y. Shi, Z. Yu, and S. Fan, "Limitations of nonlinear optical isolators due to dynamic reciprocity," *Nature Photon.*, vol. 9, no. 6, pp. 388–392, 2015.

[12] F. Nazari, N. Bender, H. Ramezani, M. Moravvej-Farshi, D. Christodoulides, and T. Kottos, "Optical isolation via pt-symmetric nonlinear fano resonances," *Opt. Exp.*, vol. 22, no. 8, pp. 9574–9584, 2014.

[13] Z. Yu and S. Fan, "Complete optical isolation created by indirect interband photonic transitions," *Nature Photon.*, vol. 3, no. 2, pp. 91–94, 2009.

[14] K. Fang, Z. Yu, and S. Fan, "Photonic Aharonov-Bohm effect based on dynamic modulation," *Phys. Rev. Lett.*, vol. 108, no. 15, 2012, Art. no. 153901.

[15] I. A. Williamson and S. Fan, "Broadband optical switch based on an achromatic photonic gauge potential in dynamically modulated waveguides," *Phys. Rev. Appl.*, vol. 11, no. 5, 2019, Art. no. 054035.

[16] C. R. Doerr, N. Dupuis, and L. Zhang, "Optical isolator using two tandem phase modulators," *Opt. Lett.*, vol. 36, no. 21, pp. 4293–4295, 2011.

[17] Q. Lin, J. Wang, and S. Fan, "Compact dynamic optical isolator based on tandem phase modulators," *Opt. Lett.*, vol. 44, no. 9, pp. 2240–2243, 2019.

[18] A. Y. Song, Y. Shi, Q. Lin, and S. Fan, "Direction-dependent parity-time phase transition and nonreciprocal amplification with dynamic gain-loss modulation," *Phys. Rev. A*, vol. 99, no. 1, 2019, Art. no. 013824.

[19] Y. Shi, Q. Lin, M. Minkov, and S. Fan, "Nonreciprocal optical dissipation based on direction-dependent rabi splitting," *IEEE J. Sel. Topics Quantum Electron.*, vol. 24, no. 6, Nov./Dec. 2018, Art. no. 3500107.

[20] D. L. Sounas and A. Alu, "Angular-momentum-biased nanorings to realize magnetic-free integrated optical isolation," *ACS Photon.*, vol. 1, no. 3, pp. 198–204, 2014.

[21] D. L. Sounas, C. Caloz, and A. Alu, "Giant non-reciprocity at the subwavelength scale using angular momentum-biased metamaterials," *Nature Commun.*, vol. 4, 2013, Art. no. 2407.

[22] A. Mock, "Optical isolation using compact time-modulated cavity array," in *Proc. Int. Appl. Comput. Electromagnetics Soc. Symp.*, 2020, pp. 1–2.

[23] A. Mock, D. Sounas, and A. Alù, "Magnet-free circulator based on spatiotemporal modulation of photonic crystal defect cavities," *ACS Photon.*, vol. 6, no. 8, pp. 2056–2066, 2019.

[24] A. Mock, "Compact magnetless optical isolator using two coupled microcavities with time-modulation," in *Proc. Int. Appl. Comput. Electromagnetics Soc. Symp.*, 2021, pp. 1–4.

[25] I. Cardea et al., "Arbitrarily high time bandwidth performance in a nonreciprocal optical resonator with broken time invariance," *Sci. Rep.*, vol. 10, no. 1, 2020, Art. no. 15752.

[26] K. L. Tsakmakidis et al., "Breaking lorentz reciprocity to overcome the time-bandwidth limit in physics and engineering," *Science*, vol. 356, no. 6344, pp. 1260–1264, 2017.

[27] H. Lira, Z. Yu, S. Fan, and M. Lipson, "Electrically driven nonreciprocity induced by interband photonic transition on a silicon chip," *Phys. Rev. Lett.*, vol. 109, no. 3, 2012, Art. no. 033901.

[28] H. Tian et al., "Magnetic-free silicon nitride integrated optical isolator," *Nature Photon.*, vol. 15, no. 11, pp. 828–836, 2021.

[29] A. Pandey, S. Dwivedi, T. Zhenzhou, S. Pan, and D. Van Thourhout, "Nonreciprocal light propagation in a cascaded all-silicon microring modulator," *ACS Photon.*, vol. 8, no. 7, pp. 1997–2006, 2021.

[30] A. Zarif, K. Mehrany, M. Memarian, and H. Heydarian, "Optical isolation enabled by two time-modulated point perturbations in a ring resonator," *Opt. Exp.*, vol. 28, no. 11, pp. 16805–16821, 2020.

[31] A. Zarif, M. Memarian, and K. Mehrany, "Rigorous derivation of temporal coupled-mode theory expressions for travelling and standing wave resonators coupled to optical waveguides," in *Proc. 7th Int. Conf. Photon., Opt., Laser Technol.*, 2019, vol. 1, pp. 201–208.

[32] S. Fan, W. Suh, and J. D. Joannopoulos, "Temporal coupled-mode theory for the fano resonance in optical resonators," *J. Opt. Soc. Amer. A*, vol. 20, no. 3, pp. 569–572, 2003.

[33] N. M. Wereley, "Analysis and control of linear periodically time varying systems," Ph.D. dissertation, MIT Press, Cambridge, MA, USA, 1990.

[34] R. Soref and B. Bennett, "Electrooptical effects in silicon," *IEEE J. Quantum Electron.*, vol. QE-23, no. 1, pp. 123–129, Jan. 1987.

[35] D. Gray et al., "Thermo-optic multistability and relaxation in silicon microring resonators with lateral diodes," *Phys. Rev. Appl.*, vol. 14, Aug. 2020, Art. no. 024073. [Online]. Available: https://link.aps.org/doi/10.1103/PhysRevApplied.14.024073